

# Impact of Iron Precipitation on Phosphorus-Implanted Silicon Solar Cells

Hannu S. Laine, Ville Vähänissi, Ashley E. Morishige, Jasmin Hofstetter, Antti Haarahiltunen, Barry Lai, Hele Savin, and David P. Fenning

**Abstract**—Ion implantation is a promising method to implement a high-performance emitter for crystalline silicon solar cells. However, an implanted emitter redistributes and mitigates harmful metal impurities to a different degree than a diffused one. This paper quantitatively assesses the effect of iron contamination level on the bulk diffusion length and open-circuit voltage of phosphorus-implanted solar cells manufactured with varying gettering parameters. By synchrotron-based micro-X-ray fluorescence measurements, we directly observe a process-dependent iron precipitate size distribution in the implanted emitters. We show that controlling the iron precipitate size distribution is important when optimizing final cell performance and discover a tradeoff between large shunting precipitates in the emitter and a high density of recombination active small precipitates in the wafer bulk. We present a heterogeneous iron precipitation model capable of reproducing the experimentally measured size distributions. We use the model to show that the dominant gettering mechanism in our samples is precipitation and that implanted emitters with surface phosphorus concentrations around  $2 \times 10^{19} \text{ cm}^{-3}$  induce little-to-no segregation-based gettering. Based on this finding, we discuss optimal gettering strategies for industrial silicon solar cells with implanted emitters.

**Index Terms**—Gettering, ion implantation, iron, modeling, precipitation, silicon, solar cell.

Manuscript received July 31, 2015; accepted May 30, 2016. The work of the authors from Aalto University was supported by the Finnish Technology Agency under the projects “PASSI” (project No. 2196/31/2011) and “NANOSOLAR” (project No. 1109/31/2012). The work of the authors from the Massachusetts Institute of Technology was supported by the National Science Foundation (NSF) and the Department of Energy under NSF CA No. EEC-1041895. Use of the Advanced Photon Source at Argonne National Laboratory was supported by the U.S. Department of Energy, Office of Science, Office of Basic Energy Sciences, under Contract DE-AC02-06CH11357. The work of H. S. Laine was supported by the Finnish Cultural Foundation and the Fulbright-Technology Industries of Finland Grant. The work of A. E. Morishige was supported by the Department of Defense through the NDSEG fellowship program. The work of D. P. Fenning was supported by the University of California San Diego Start-Up Funds.

H. S. Laine, V. Vähänissi, A. Haarahiltunen, and H. Savin are with the Department of Micro- and Nanosciences, Aalto University, 02150 Espoo, Finland (e-mail: hannu.laine@aalto.fi; ville.vahanissi@aalto.fi; antti.haarahiltunen@aalto.fi; hele.savin@aalto.fi).

A. E. Morishige is with the Massachusetts Institute of Technology, Cambridge, MA 02139 USA. (e-mail: aemorish@alum.mit.edu).

J. Hofstetter was with the Massachusetts Institute of Technology, Cambridge, MA 02139 USA. She is now with 1366 Technologies, Inc., Bedford, MA 01730 USA (e-mail: jasmin.hofstetter@gmx.de).

B. Lai is with the Advanced Photon Source, Argonne National Laboratory, Argonne, IL 60439 USA (e-mail: blai@aps.anl.gov).

D. P. Fenning was with the Massachusetts Institute of Technology, Cambridge, MA 02139 USA. He is now with the Department of Nanoengineering, University of California San Diego, La Jolla, CA 92093 USA (e-mail: dfenning@eng.ucsd.edu).

Color versions of one or more of the figures in this paper are available online at <http://ieeexplore.ieee.org>.

## I. INTRODUCTION

IMPLANTATION is interesting to the silicon solar cell industry as a pathway to the realization of a high-performance emitter. Ion implantation offers numerous benefits over the traditional dopant in-diffusion, such as 1) higher blue response and lower surface recombination velocity with easy fine-tuning of the dopant profile [1], [2]; 2) possible reduction in processing steps through *in-situ* oxide passivation and the avoidance of phosphorus-silicate glass and laser edge isolation [1], [3]; 3) high run-to-run and wafer-to-wafer homogeneity thanks to precise spatial control of dopants [4], [5]; and 4) streamlined process into advanced solar cell architectures [3], [6], [7].

On the other hand, a key benefit of dopant in-diffusion, i.e., the segregation of deleterious metal impurities to the doped layer, is not necessarily present in an implanted emitter. For the case of iron with phosphorus-diffused emitters, the segregation effect appears to be caused by reactions involving vacancies [8]–[10], oxygen [11], [12], and inactive phosphorus [13], [14]. An implanted emitter typically contains less inactive phosphorus [15] and, with the avoidance of a phosphosilicate glass, possibly less vacancies and oxygen as well [12]. Ion implantation may also cause parasitic metal contamination in and of itself [16]. Further understanding of the gettering mechanisms of an implanted emitter is thus needed to achieve an effective gettering process, as has been demonstrated for diffused emitters [17], [18].

Preliminary results suggest indeed that, under certain circumstances, implantation getters iron less effectively than diffusion [1], [19] and shows signs of iron precipitation [19], [20], which has also been observed after high-energy implants used by the integrated circuit industry [21]–[23]. This paper presents a systematic study of the effect of iron contamination level and gettering parameters on phosphorus-implanted solar cell performance, with a particular emphasis on the behavior and effect of iron-silicide precipitates in the cells. This is an enhanced paper based on earlier work [24]. Earlier, we reported qualitative results of synchrotron-based micro-X-ray fluorescence ( $\mu$ -XRF) measurements on the precipitate size distributions of implanted cells. This paper presents quantified  $\mu$ -XRF data and compares the iron precipitate distributions to macroscopic solar cell properties, such as bulk minority carrier diffusion length ( $L_{\text{diff}}$ ) and open-circuit voltage ( $V_{\text{OC}}$ ). Additionally, we investigate the dominant gettering mechanism of an implanted emitter by comparing simulation results from a heterogeneous iron precipitation model [25] with a phosphorus-related segregation

TABLE I  
GETTERING ANNEALS PERFORMED IN THIS STUDY

Sample	Gettering anneal
800 °C	Slow cool* + 2 h at 800 °C
750 °C	Slow cool* + 3.5 h at 750 °C
620 °C	Slow cool* + 8 h at 620 °C
RT+620 °C	Pullout to room temperature (RT) at 895 °C + 8 h at 620 °C

\* 4 °C/min at  $T > 800$  °C, 2 °C/min at  $T \leq 800$  °C.

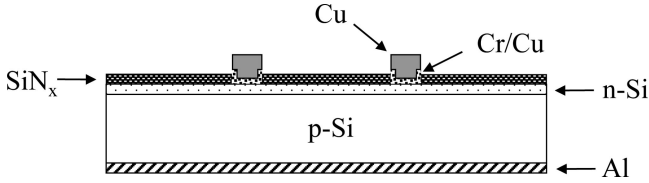


Fig. 1. Cell architecture used in this study.

gettering model for iron [8]. Leveraging our simulation findings, we discuss how to best utilize precipitation-based gettering in the manufacturing of industrial ion-implanted silicon solar cells.

## II. EXPERIMENTAL GETTERING STUDY

### A. Sample Preparation and Characterization Methods

Four hundred- $\mu\text{m}$ -thick, 3- $\Omega\text{-cm}$ , p-type electronic-grade Cz-silicon wafers with a low oxygen level (7–9 ppma) were intentionally contaminated [26] with 1) a medium iron level of  $1 \times 10^{13} \text{ cm}^{-3}$ , 2) a high iron level of  $2 \times 10^{14} \text{ cm}^{-3}$ , or 3) left without intentional contamination. After contamination, the front side of the wafers was patterned via oxidation, lithography, and buffered HF to form seven  $2 \times 2 \text{ cm}^2$  cells per wafer. The wafers were ion implanted on the front side through a 31-nm-thick screen oxide with a phosphorus dose of  $10^{15} \text{ cm}^{-2}$  at 50 keV. The screen oxide was removed by etching and the implant annealed at 1000 °C for a total of 40 min, which was followed by one of the four gettering anneals described in Table I. The implant anneal temperature is higher than the iron in-diffusion temperature [26], guaranteeing that all iron is fully dissolved prior gettering and enabling a physically accurate initial condition for subsequent simulations. The sheet resistances after the gettering anneals were measured by a four-point probe to be between 85 and 96  $\Omega/\square$  [19].

The solar cell process continued with an identical process as used in [26], except in this study, Cr/Cu contacts were used instead of Ti/W. The cell architecture is illustrated in Fig. 1. The Cu fingers were electroplated on one cell from each wafer.  $I$ - $V$  curves of the electroplated cells were measured in the dark and under standard illumination conditions (AM1.5G, 1000  $\text{W}\cdot\text{m}^{-2}$ , 25 °C) with the irradiance decay cell analysis method [27]. Open-circuit voltages of the nonplated cells were measured to assess the reproducibility of the cell process. The  $V_{OC}$  standard deviations within each wafer were found to be at most 4%, and thus, only mean values for  $V_{OC}$  are reported in this study. The contacting process used in this study is not optimized for the low surface P concentration of the emitters ( $\sim 2 \times 10^{19} \text{ cm}^{-3}$  [19]),

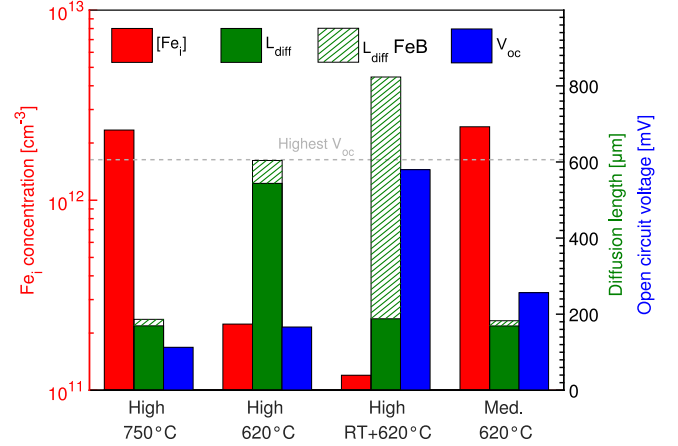


Fig. 2. Measured interstitial iron concentration ( $[\text{Fe}_i]$ ), diffusion length ( $L_{\text{diff}}$  SPV) before dissociating the iron–boron pairs [19], and open-circuit voltage ( $V_{OC}$ ) are shown for selected samples. Additionally, the low-injection diffusion length imposed by the iron boron pairs through SRH recombination ( $L_{\text{diff FeB}}$ ) is shown.

and current losses were dominated by high series resistance ( $\sim 7 \Omega\cdot\text{cm}^2$ ). Thus, cell parameters other than  $V_{OC}$  and  $L_{\text{diff}}$  are not discussed in this paper.

To study  $L_{\text{diff}}$  and bulk interstitial iron concentration ( $[\text{Fe}_i]$ ) response to gettering, a set of reference wafers without the cell structure was similarly implanted and identically gettered for all contamination levels and all gettering anneals. After the gettering anneals,  $L_{\text{diff}}$  and  $[\text{Fe}_i]$  were measured from the reference wafers using the surface photovoltage (SPV) method [26]. These results have been reported earlier in [19].

$\mu$ -XRF was performed on the emitter side of selected samples at the advanced photon source beamline 2-ID-D [28] with a 220-nm step size and 10-keV incident photon energy. The effective information depth of the sample and detector geometry was 8.8  $\mu\text{m}$  for iron  $K_{\alpha}$  radiation. The data were quantified using NIST-traceable 1832 and 1833 standards. The precipitate size distribution was analyzed using a previously reported approach [29], [30], with a noise cutoff for each pixel value less than  $\mu + 3.5\sigma$ , where  $\mu$  is the mean and  $\sigma$  the standard deviation of a fitted iron loading noise distribution. The total number of iron atoms in each precipitate was counted by summing over each pixel contained within an individual cluster. The quantification algorithm assumes the  $K_{\alpha}$  radiation to originate at the sample surface, which underestimates the number of Fe atoms in precipitates below the surface. Earlier secondary ion mass spectrometry (SIMS) measurements found iron to be mostly located in the first 100 nm of the samples studied here [19]; therefore, this error remains small. The quantified precipitate sizes are estimated to be accurate to within a factor of 2 [30].

### B. Postgettering Bulk $[\text{Fe}_i]$ Does Not Always Predict Cell Performance

Our previous work on intentionally contaminated Cz-Si solar cells with diffused emitters has shown that final solar cell performance is mostly affected by the residual dissolved iron concentration [26]. This paper focuses on four cells, which show

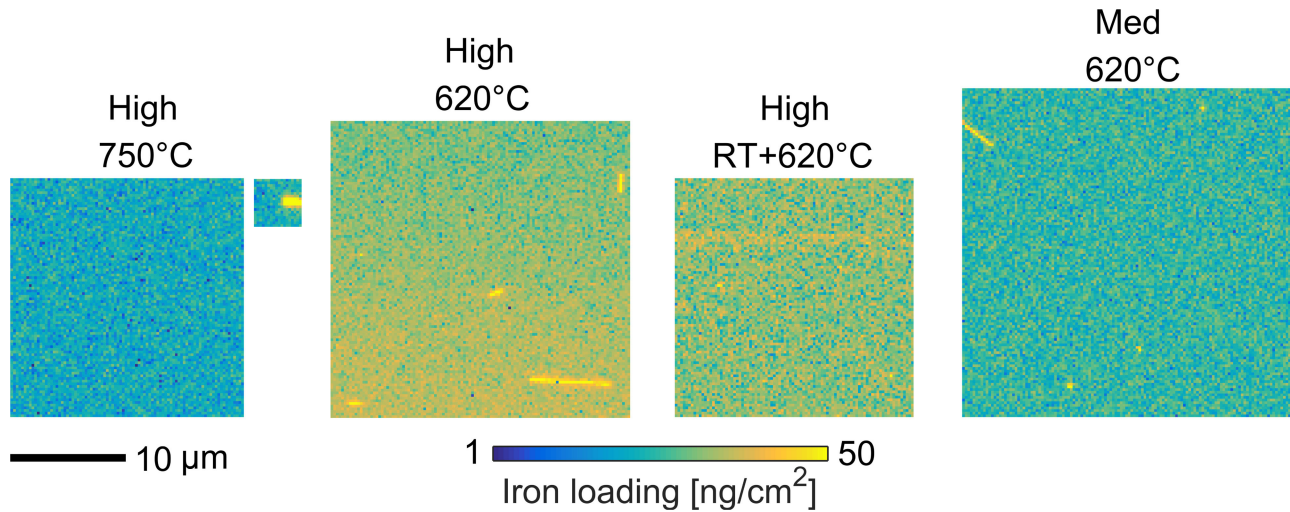


Fig. 3. Iron load on a logarithmic scale measured by  $\mu$ -XRF from the highly contaminated 750 °C, 620 °C, and RT+620 °C samples and from the mediumly contaminated 620 °C sample are shown.

a stark contrast with this trend: the highly contaminated 750 °C, 620 °C, and RT+620 °C samples, as well as the mediumly contaminated 620 °C sample. Fig. 2 compares postgettering  $[\text{Fe}_i]$  and  $L_{\text{diff}}$  values before the dissociation of iron–boron pairs, as well as  $V_{\text{OC}}$  values of finished devices and **calculated low-injection  $L_{\text{diff}}$  values imposed by the FeB pairs through Shockley–Read–Hall (SRH) recombination [31]** for these four samples. The highly contaminated 750 °C and 620 °C samples exhibit varying efficacy at removing interstitial iron from the wafer bulk resulting in different bulk diffusion lengths of 169 and 544  $\mu\text{m}$ , respectively, which are both close to the iron-related diffusion length limit in the corresponding samples (186 and 604  $\mu\text{m}$ , respectively). The mediumly contaminated 620 °C sample has almost identical bulk  $[\text{Fe}_i]$  as the highly contaminated 750 °C sample, and its  $L_{\text{diff}}$  is similarly mostly limited by FeB pairs. However, the diffusion length of the RT+620 °C sample (188  $\mu\text{m}$ ) is considerably lower than the FeB-limited  $L_{\text{diff}}$  (823  $\mu\text{m}$ ).

In general, open-circuit voltage is affected by the minority carrier diffusion length [32]. Interestingly, the measured open-circuit voltages of completed devices do not correlate with the measured diffusion lengths. The highly contaminated 750 °C and 620 °C samples and the mediumly contaminated 620 °C are barely functioning solar cells with sub-250-mV  $V_{\text{OC}}$  values, while the RT+620 °C sample delivers an  $V_{\text{OC}}$  approaching 600 mV, close to the highest  $V_{\text{OC}}$  measured from the noncontaminated reference cells (gray line, Fig. 2). **We hypothesize that the low  $L_{\text{diff}}$  of the RT+620 °C sample is caused by a high density of iron precipitates in the bulk and the low  $V_{\text{OC}}$  values of the other three samples by large precipitates in the emitter causing shunts.**

### C. Large Precipitates Found From Low $V_{\text{OC}}$ Cells

To investigate the root cause for the sub-250-mV  $V_{\text{OC}}$  values reported in Section II-B, Fig. 3 shows the quantified Fe  $K_{\alpha}$  fluorescence maps of the four samples discussed in Fig. 2. Precipitates are found in each sample, but their size distribution

strongly depends on the annealing treatment. In the area of 416  $\mu\text{m}^2$  measured from the highly contaminated 750 °C sample, a single precipitate or precipitate cluster emerges. It is sizable, with a length of 1.6  $\mu\text{m}$  directly estimated from the map. A low density of precipitates is expected because of the slow ramp to the gettering anneal and the relatively high iron solubility at 750 °C ( $1.9 \times 10^{12} \text{ cm}^{-3}$ ), which inhibits widespread nucleation.

In the 620 °C samples, on the other hand, the slow ramp continues to 620 °C (solubility  $8.4 \times 10^{10} \text{ cm}^{-3}$ ), which results in higher supersaturation and, eventually, stronger precipitation. The  $\mu$ -XRF map of the highly contaminated 620 °C sample correspondingly contains small barely visible precipitates as well as several larger precipitates. The smallest precipitates fit within a single 220-nm pixel, while the largest spans almost 7  $\mu\text{m}$  in length. In addition, the aspect ratio of the largest precipitate or agglomerate in the highly contaminated 620 °C sample approaches 15:1. The mediumly contaminated 620 °C sample exhibits similar behavior as the highly contaminated 620 °C sample, showing one large precipitate approximately 2.3  $\mu\text{m}$  in size, as well as several smaller ones. The precipitates are, on average, smaller, in the mediumly contaminated than the highly contaminated 620 °C sample, due to the lower total amount of iron present in the sample.

The precipitates in these three samples exhibit anisotropic growth, appearing to be either plate- or needle-like. Similar, several micrometers long needle-like  $\alpha$ -FeSi<sub>2</sub> precipitates have recently been found at prebreakdown sites of multicrystalline silicon solar cells [33], as well as earlier in silicon transistors [34]. These very large (several micrometers) precipitates have the capacity to short-circuit the emitter [35] and are a likely cause for the low  $V_{\text{OC}}$  measured from these three cells (cf., Fig. 2). Shunting is also supported by superlinear reverse bias currents measured in the dark (not shown) from the low  $V_{\text{OC}}$  cells. At  $-1 \text{ V}$ , the three low  $V_{\text{OC}}$  cells showed current densities between 4 and 14  $\text{mA}/\text{cm}^2$ , whereas the nine other cells manufactured showed reverse current densities of at most 4  $\mu\text{A}/\text{cm}^2$ .



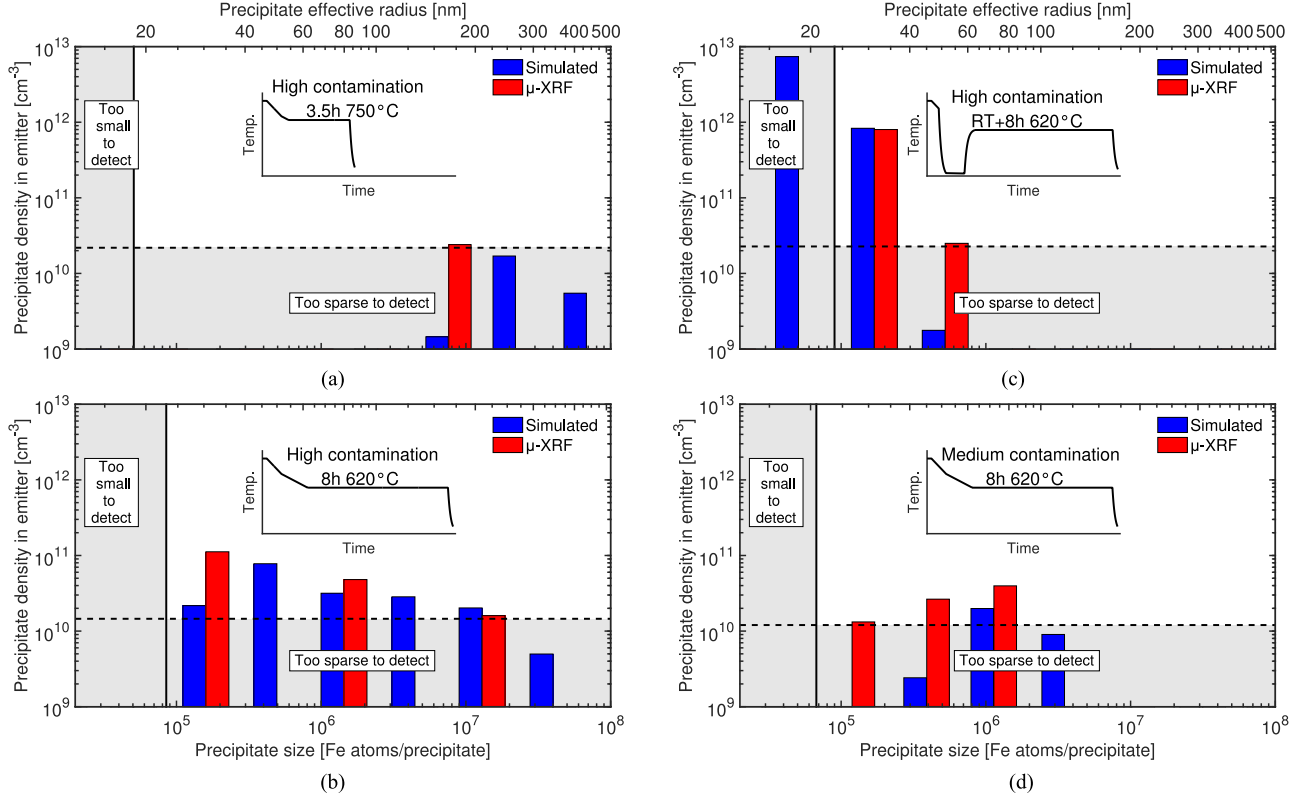


Fig. 4. Comparison of the simulated and measured iron precipitate size distributions in the emitter of the highly contaminated (a) 750 °C, (b) 620 °C, and (c) the RT+620 °C samples, as well as (d) the mediumly contaminated 620 °C sample. The upper  $x$ -axis shows the effective radius of the precipitates given by (1). In addition, the minimum detectable size and the minimum detectable density are shown. The RT pullout is simulated as an exponential cool down to room temperature with a time constant of 9 min. The depth of the precipitate-containing layer is assumed to be 100 nm, as measured by SIMS [19]. The time–temperature profile of each sample is shown in the inset.

Superlinear reverse bias currents have been attributed to iron precipitates forming an ohmic contact with the  $n$ -type emitter and a Schottky junction with the  $p$ -type base [33], [36].

As opposed to the other samples, the RT+620 °C sample experienced strong nucleation during the room temperature pullout, when the supersaturation of iron was high but the diffusivity low. The strong nucleation translated into a high density of precipitates during the 8-h gettering anneal: The 400- $\mu\text{m}^2$  map contains many (33 in total) small precipitates, most of which are only slightly above the background noise limit and fit within a single 220-nm pixel. With more precipitates acting as sinks for iron in the RT+620 °C than in the 620 °C samples, the individual precipitates did not grow as large in the RT+620 °C sample, as in either of the 620 °C samples. It seems that here, the precipitates remained small enough to leave the emitter intact, not compromising the cells'  $V_{OC}$ .

### III. UNDERSTANDING THE GETTERING MECHANISM AND LIFETIME OPTIMIZATION BY SIMULATION

#### A. Precipitation-Based Gettering Model

In silicon photovoltaics, there are two main gettering mechanisms for interstitial iron and other dissolved impurities. The first is the segregation of impurities due to dopant-induced solubility differences within the wafer [37], [38]. The second one is supersaturation-driven precipitation, also known as “relaxation

gettering,” which, for iron, typically comprises the formation of iron-silicide clusters [38]–[41]. Precipitation can occur, for example, at extended bulk defects, oxygen precipitates, or at interfaces [39], [42], [43]. In this study, we investigate a gettering model where the reduction of interstitial iron from the wafer bulk is solely explained through precipitation and compare it to a phosphorus-induced point-defect segregation model [8].

In our precipitation-based gettering model, the nucleation and evolution of iron precipitates during wafer processing is studied by means of a Fokker–Planck equation-based precipitation model [25]. The model simulates potential nucleation sites with a density  $N_{\text{site}}$  throughout the wafer. Once nucleated, the effective radii  $r_{\text{eff}}$  of the precipitates grow as

$$r_{\text{eff}} = r_0 + 5.1 \times 10^{-9} [\text{cm}] n^{1/2} \quad (1)$$

where  $r_0$  describes the empty precipitation site and the  $n$ -dependent term describes the growing precipitate, where  $n$  is the number of Fe atoms in each precipitate [20].

This study incorporates the recent iron solubility data measured by Murphy and Falster at temperatures below 800 °C [44]. To maintain consistency to previous work, this required refitting the lumped simulation parameter  $E_a$ , which accounts for all energetic changes related to precipitate nucleation and growth, such as surface energy and matrix strain [25], [45]. The simulation parameters  $r_0$ ,  $N_{\text{site}}$ , and  $E_a$  are described in detail in the Appendix.

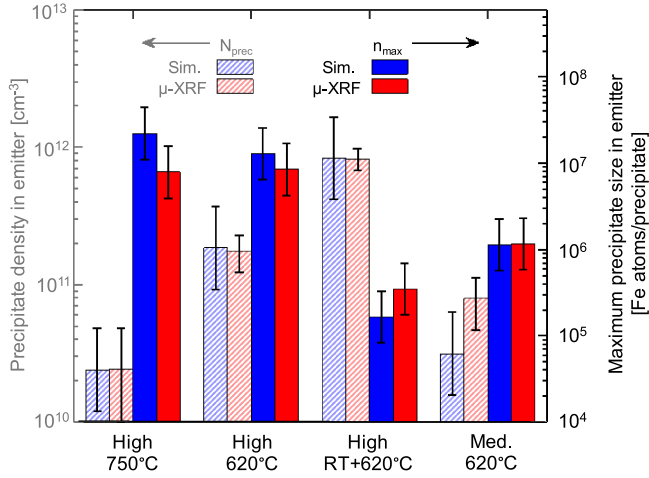


Fig. 5. Measured and simulated precipitate densities and maximum precipitate sizes for the samples probed with  $\mu$ -XRF with estimated error limits.

The  $L_{\text{diff}}$  limit imposed by precipitates is calculated assuming a precipitate radius set by (1) using a recombination model based on thermionic emission at the precipitate–silicon interface. The model was first implemented by Tan *et al.* [46], [47] and parameterized by Kwail *et al.* [48]. Electrical properties of iron–boron pairs and interstitial iron are assumed as in [49]. General properties of charge carriers in silicon are modeled as in [50] and [51].

### B. Experimental Precipitate Size and Density Trends Reproduced by Precipitation-Only Model

First, we simulated the precipitate size distributions in the emitter after each gettering process for both highly and mediumly contaminated samples. We compared the results to the  $\mu$ -XRF results. Fig. 4 shows that the simulations and  $\mu$ -XRF results predict similar trends. In the highly contaminated 750 °C sample, both simulations and measurements show a low density of large precipitates. In the 620 °C samples, the supersaturation during processing was higher than in the 750 °C sample, which resulted in stronger precipitation. In the 620 °C samples, the largest precipitates are, thus, almost as large as the precipitates in the 750 °C sample, but the 620 °C samples contain notably higher densities of smaller precipitates as well. Simulations also reproduce the high density of precipitates in the emitter found from the highly contaminated RT+620 °C sample. Additionally, the simulations show the RT+620 °C sample having the highest density of precipitates in the bulk, which is in line with our hypothesis in Section II-B.

Fig. 5 shows that within the uncertainty in both simulated and measured precipitate sizes and densities, the simulated maximum precipitate size  $n_{\text{max}}$  and precipitate density  $N_{\text{prec}}$  match the experimental values in all four samples, suggesting that the model can be used to benchmark the impact of iron contamination levels under different solar cell processes. The maximum precipitate size  $n_{\text{max}}$  is essentially the rightmost bar in Fig. 4, which is defined to be the largest precipitate size, with a precipitate density of at least  $1.4 \times 10^{10} \text{ cm}^{-3}$ , corresponding to a

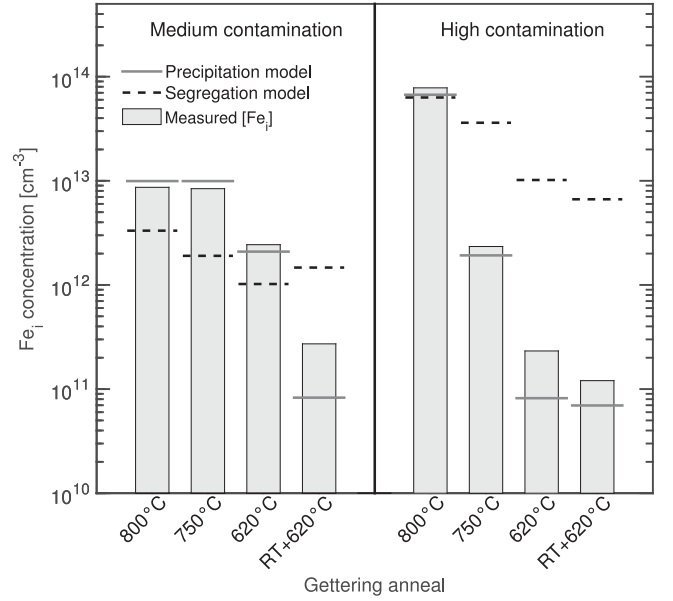


Fig. 6. Measured residual bulk  $[\text{Fe}_i]$  after various gettering anneals compared with the respective values simulated by a precipitation-based gettering model (solid lines) and a segregation-based model (dashed lines).

density of one precipitate in a  $25 \times 25 \mu\text{m}^2$  map. The precipitate density  $N_{\text{prec}}$ , on the other hand, corresponds to the sum of the bars above the size detection limit in Fig. 4. For the experimental  $N_{\text{prec}}$ , the uncertainty was estimated as  $\sqrt{N}$ , where  $N$  is the number of precipitates found in each sample.

### C. Precipitation Dominates Over Segregation Gettering

In addition to reproducing the precipitate size distributions, the precipitation-based gettering model accurately captures the interstitial Fe gettering efficiencies of all gettering anneals, which implies that precipitation is the dominant gettering mechanism. This is evident in Fig. 6, which shows the residual bulk interstitial iron concentrations after the gettering anneals [19]. We also show the calculated gettering efficiencies assuming the phosphorus profile measured by SIMS [19] and the iron segregation and segregation model from [8]. The simulated values by precipitation and segregation are shown as solid and dashed lines, respectively, in Fig. 6. The trends predicted by the segregation model do not explain the observed gettering efficiencies. For example, the segregation model predicts mostly stronger-than-observed gettering for the mediumly contaminated samples, whereas the calculated gettering efficiency for the highly contaminated samples is over an order of magnitude too small in three out of the four samples. The segregation model also predicts a lower gettering efficiency for the mediumly contaminated RT+620 °C sample than for the mediumly contaminated 620 °C sample, even though approximately an order of magnitude smaller  $[\text{Fe}_i]$  was measured from the RT+620 °C sample. This is well explained by the precipitation model, because the room temperature pullout is extremely favorable for nucleation and, thus, creates more iron precipitates to act as sinks for  $\text{Fe}_i$ .

In conclusion, the gettering efficiencies simulated by the precipitation model and the simulated precipitate size distributions

agree with the measured iron distributions (cf., Figs. 4–6). This supports our assumption of negligible phosphorus-related segregation occurring in these samples. Thus, effective segregation gettering appears to be compromised in implanted emitters with  $[P_{\text{surf}}] \approx 2 \times 10^{19} \text{ cm}^{-3}$ . In principle, this result may hold for diffused emitters as well. Segregation gettering is important because it does not require a supersaturation of contaminants, as is required to drive precipitation, but instead works on all contamination levels. To our knowledge, quantitative gettering tests with intentionally contaminated samples have not been performed previously on such lowly doped emitters.

#### D. Processing Must Optimize Iron Precipitate Nucleation

We have thus far demonstrated good agreement between the model and the experimentally measured values for both precipitated and interstitial iron concentrations for all processes. Leveraging this agreement, we calculated the  $L_{\text{diff}}$  imposed by iron precipitates (excluding recombination due to  $\text{Fe}_i$ ) to investigate the cause for the non- $\text{Fe}_i$ -limited bulk  $L_{\text{diff}}$  experimentally observed in the highly contaminated RT+620 °C sample (cf., Fig. 2). The model correctly predicts the lowest precipitate limited low-injection  $L_{\text{diff}}$  of 817  $\mu\text{m}$  for the highly contaminated RT+620 °C as compared with 1216, 4800, and 2215  $\mu\text{m}$  calculated for the highly contaminated 620 °C and 750 °C samples and the mediumly contaminated 620 °C sample, respectively. However, the calculated diffusion length of the highly contaminated RT+620 °C sample (817  $\mu\text{m}$ ) is still approximately a factor of 4 higher than the one measured with SPV (188  $\mu\text{m}$ , cf., Fig. 2). Likely causes for the discrepancy are 1) the used parameterization of the precipitate recombination model [48] assumes the precipitates to be spread along dislocation lines. Allowing the precipitates to be independently spread in all three dimensions would increase their impact on carrier recombination. 2) Another cause is the simplistic assumption that the bulk precipitation sites are described by the same capture radius  $r_0$  as the precipitation sites in the emitter.

Thus, we have identified two critical trends during iron point defect removal from the bulk: Large precipitates can shunt the emitter (cf., Section II-C), and a high density of precipitates in the bulk can limit bulk  $L_{\text{diff}}$ . An optimal process would thus nucleate a medium density of precipitates in the emitter, providing adequate sinks for rapid iron point defect removal and preventing individual precipitates from growing detrimentally large, while simultaneously keeping the density of bulk precipitates low enough to not limit  $L_{\text{diff}}$ . For the iron concentrations used in this study, this could possibly be achieved with a relatively fast ramp of approximately 10 °C/min from the implant activation anneal to the gettering anneal.

#### E. Optimizing Gettering as a Function of Iron Concentration

Having established that the lifetime simulation accurately predicts trends, we simulated the level of contamination required to activate the relaxation gettering mechanism in implanted emitters. As precipitation requires a certain level of impurity supersaturation to occur, the significance of contamination level is enhanced with precipitation-based gettering. We simulated two

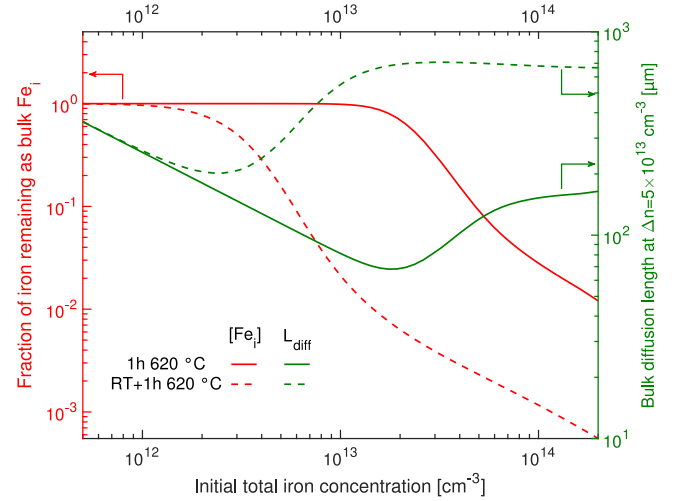


Fig. 7. Simulated gettering efficiencies attributed to precipitation, as well as precipitate-limited bulk diffusion lengths for a range of iron contamination levels.

emitter formation processes under iron contamination levels ranging from  $5 \times 10^{11}$  to  $2 \times 10^{14} \text{ cm}^{-3}$ . The simulated emitter processes comprised of the implantation anneal used in this study followed by 1) a slow cool, or 2) an RT pullout at 895 °C and a reheating to a 1-h anneal at 620 °C, with an industrial wafer thickness of 160  $\mu\text{m}$ . These gettering anneals correspond to higher throughput versions of the “620 °C” and “RT+620 °C” processes studied experimentally in this paper. Fig. 7 presents the fraction of total iron remaining as  $\text{Fe}_i$  in bulk after processing (gettering efficiency) as well as the calculated  $L_{\text{diff}}$  after the process, assuming all the dissolved iron is in interstitial state and accounting for the recombination activity of bulk precipitates as well. Here, we used an injection level of  $\Delta n = 5 \times 10^{13} \text{ cm}^{-3}$ , which is a typical injection level for a high-performance p-type passivated emitter rear contact (PERC) device [52].

It can be seen that precipitation-based gettering begins to play a role above contamination levels of  $5 \times 10^{11} \text{ cm}^{-3}$  for the RT process and above  $1 \times 10^{13} \text{ cm}^{-3}$  for the slow cool process. The advantage of the RT process is a higher density of precipitates in the emitter, which getter iron more effectively. The gettering efficiency increases with contamination level, suggesting that precipitation effectively “compensates” for a higher contamination level. For the contamination level range studied, maximum calculated bulk diffusion length reached by either of the processes is 709  $\mu\text{m}$  (162- $\mu\text{s}$  lifetime), which could yield an approximately 21%-efficient PERC device, according to device simulations [52]. However, this is likely to be an optimistic estimate, as the measured  $L_{\text{diff}}$  in the experimentally studied highly contaminated RT+620 °C sample is lower than the corresponding simulated  $L_{\text{diff}}$  imposed by bulk precipitates in that sample. However, many solar cell processes naturally contain additional iron mitigation, for example, in the form of hydrogenation [53], [54] or gettering during contact firing [55]. Thus, our simulations indicate that with careful process design, an implanted emitter is capable of enabling highly performing devices comprised of relatively contaminated starting material.

Further work should aim to elucidate the impact of varying surface phosphorus concentration and/or implantation parameters on our model. It is possible that a higher surface phosphorus concentration could activate segregation-based gettering in an implanted emitter as well. Likewise, we expect the density, and possibly also the capture radius, of the precipitation sites in the emitter to be dependent on the implant energy, dose, and the activation anneal.

#### IV. CONCLUSION

In traditional phosphorus-diffused emitters, the removal of iron point defects from the bulk is largely attributed to an increased iron solubility in the phosphorus-diffused region compared with the boron-doped bulk. In this study, we studied implanted phosphorus emitters with surface phosphorus concentration around  $2 \times 10^{19} \text{ cm}^{-3}$ , for which the gettering effect of dissolved iron upon various gettering anneals could be explained through a purely precipitation-based model. We showed that during precipitation-based gettering, not only iron point defect removal from the wafer bulk is important, but also the evolution of iron precipitate size distribution. Large precipitates in the emitter can shunt the emitter, and a high density of precipitates in the bulk can limit the minority carrier diffusion length, even in material with a low density of intrinsic structural defects. By performing  $\mu$ -XRF measurements after varying gettering anneals, we showed that the precipitate size distribution can be controlled by different temperature treatments. We describe a simulation tool that can be used to design cell processes that optimize the precipitate size distribution to maximize solar cell performance.

#### APPENDIX

##### ASSESSMENT OF SIMULATION PARAMETERS

In addition to the established values of iron diffusivity [56] and iron solubility [44], [57], the model presented in this study employs the following simulation parameters: a lumped energy parameter  $E_a$ , and the capture radius  $r_0$ , and density  $N_{\text{site}}$  of precipitation sites.  $N_{\text{site}}$  is space dependent, and different values are used in the emitter ( $N_{\text{site}}^{\text{emitter}}$ ), bulk ( $N_{\text{site}}^{\text{bulk}}$ ), and at the Si-SiO<sub>2</sub> interface ( $N_{\text{site}}^{\text{Si-SiO}_2}$ ) at the back of the wafers. The width of the emitter and Si-SiO<sub>2</sub> interface region is modeled as 100 nm. The values used are listed in Table II.

##### A. Simulation Parameters Extracted From Previous Data

Including the space dependence of  $N_{\text{site}}$ , the simulator contains five initially free parameters:  $r_0$ ,  $E_a$  and  $N_{\text{site}}^{\text{emitter}}$ ,  $N_{\text{site}}^{\text{bulk}}$ , and  $N_{\text{site}}^{\text{Si-SiO}_2}$ . To reduce the number of free parameters, we extracted  $N_{\text{site}}^{\text{bulk}}$  and  $N_{\text{site}}^{\text{Si-SiO}_2}$  from earlier data based on the changes in bulk  $[\text{Fe}_i]$  measured in samples similar to the RT+620 °C samples in this study, but which were processed without implantation, leaving only the bulk and the Si-SiO<sub>2</sub> interfaces as the gettering sites. Specifically, we reproduced the data presented in [19, Fig. 5] by simulations.

We modeled the Si-SiO<sub>2</sub> interface as a 100-nm-thick layer with  $N_{\text{site}}$  of  $2 \times 10^{10} \text{ cm}^{-3}$ . The thickness of this and the emitter

TABLE II  
SIMULATION PARAMETERS

Parameter	Value
Precipitation site density $N_{\text{site}}$	$8.3 \times 10^{12} \text{ cm}^{-3}$ in emitter $3.3 \times 10^5 \text{ cm}^{-3}$ in bulk $2 \times 10^{10} \text{ cm}^{-3}$ at Si-SiO <sub>2</sub> interface
Precipitation site capture radius $r_0$	5 nm
Precipitate growth energy parameter $E_a$	$2.0 \times 10^{-4} T + 0.68 \text{ [eV]}, T \leq 500 \text{ }^\circ\text{C}$ $6.0 \times 10^{-4} T + 0.42 \text{ [eV]}, 500^\circ\text{C} < T \leq 700^\circ\text{C}$ $8.4 \times 10^{-4} T + 0.18 \text{ [eV]}, T > 700 \text{ }^\circ\text{C}$

layer can be varied between 10 and 1000 nm without essentially changing the simulation results, as long as the total amount of precipitation sites is held constant. The  $N_{\text{site}}^{\text{bulk}}$  value used ( $3.3 \times 10^5 \text{ cm}^{-3}$ ) would correspond to a dislocation density of one dislocation per  $\text{cm}^2$  using the line density of nucleation sites along a dislocation from [45]. While this number may well be unphysically low, a low density of dislocations and bulk microdefects can still be expected from the low-oxygen electronic-grade Cz-Si wafers used in the study. Because we believe these  $N_{\text{site}}^{\text{bulk}}$  and  $N_{\text{site}}^{\text{Si-SiO}_2}$  values to be independent from the implantation process, these are included also in the segregation-based gettering model used to produce the data in Fig. 6.

Similarly, the parameter  $E_a$ , which accounts for all energetic changes related to precipitate nucleation and growth, such as surface energy and matrix strain [25], [45] was also fitted independently from the data presented in this paper. Although this parameter has been estimated previously [25], a refitting was motivated by the need to use the iron solubility values measured by Murphy and Falster at temperatures below 800 °C [44]. Previously, extrapolated iron solubility values from measurements at temperatures over 800 °C [57] were used, which we hold less accurate than the more recently measured data [44]. Because the solubility of iron was an essential parameter in the estimation of  $E_a$ , the fitting was redone based on the same precipitation data (see [25, Fig. 1]) but by applying the new solubility data of [44]. As the data in [25] only extend up to 700 °C,  $E_a$  was held the same as in previous publications [20], [45], [58] for temperatures larger than 700 °C. The change in  $E_a$  is estimated to cause small ( $< 10\%$ ) changes in the simulated precipitate size distributions.

##### B. Fitting Parameters and Their Comparison to Earlier Literature

For reproduction of the central simulation results presented in this paper, the most important parameters are  $r_0$  and  $N_{\text{site}}$  in the emitter. These two parameters were fit to achieve the size distributions shown in Figs. 4 and 5, requiring the specific set of values we chose. On the other hand, the simulated gettering efficiencies shown in Fig. 6 are well replicated by a combination of  $r_0$ ,  $N_{\text{site}}^{\text{emitter}}$  values, as long as the product  $r_0^2 N_{\text{site}}^{\text{emitter}}$  is kept constant [20].

In this study, we modeled the emitter with  $N_{\text{site}}$  of  $8.3 \times 10^{12} \text{ cm}^{-3}$ . A multicrystalline silicon grain boundary was earlier



modeled as a 10- $\mu\text{m}$ -thick layer with  $N_{\text{site}}$  of  $6.7 \times 10^{13} \text{ cm}^{-3}$  [41]. This suggests that the modeled gettering efficiency of our emitter and the Si-SiO<sub>2</sub> interface is not greater than a typical grain boundary in multicrystalline silicon, which is understandable, given that the high-temperature (1000 °C) activation anneal likely cured most of the induced implantation damage.

The best reproduction of the measured size distributions was reached by setting  $r_0$  to 5 nm. Earlier modeling on iron precipitation at dislocations and grain boundaries in multicrystalline silicon (mc-Si) used a value of 15 nm [45] and reproduced the iron precipitate size distribution at grain boundaries of several multicrystalline silicon samples fairly well compared with microscopic  $\mu$ -XRF data [58]. The discrepancy in the used  $r_0$  values in this and earlier work implies that the matrix strain and distortion caused by residual implantation damage, the most likely species acting as nucleation sites in the emitters of this study, is smaller and more localized than that induced by extended defects in multicrystalline silicon. We nonetheless benchmarked our model against the 15-nm value and noted that the precipitate size distributions shifted toward larger precipitates with smaller densities by approximately a factor of 2. We use this factor of 2 as a guideline for the accuracy of our simulated size distributions.

#### ACKNOWLEDGMENT

The authors would like to acknowledge the help of M. A. Jensen, S. Castellanos, and E. Magaña with the  $\mu$ -XRF measurements and T. Buonassisi and D. Berney Needleman for helpful discussions. The provision of facilities and technical support by Aalto University at the Micronova Nanofabrication Centre is also acknowledged.

#### REFERENCES

- [1] E. Cho *et al.*, "Comparison of POCl<sub>3</sub> diffusion with phosphorus ion implantation for Czochralski and quasi-mono silicon solar cells," in *Proc. 40th IEEE Photovoltaic Spec. Conf. Rec.*, 2014, pp. 2966–2968.
- [2] H. Huang *et al.*, "An extendible beyond 20% efficiency cost-efficient bifacial cell using boron & phosphorus implantation technology and its prospects for the future production," in *Proc. 42nd IEEE Photovoltaic Spec. Conf. Rec.*, 2015, pp. 1–6.
- [3] M. Sheoran, M. Emsley, M. Yuan, D. Ramappa, and P. Sullivan, "Ion-implant doped large-area n-type Czochralski high-efficiency industrial solar cells," in *Proc. 38th IEEE Photovoltaic Spec. Conf. Rec.*, 2012, pp. 2254–2257.
- [4] V. Yelundur *et al.*, "First implementation of ion implantation to produce commercial silicon solar cells," in *Proc. 25th Eur. Photovoltaic Sol. Energy Conf. Exhib.*, 2011, p. 831.
- [5] A. Rohatgi *et al.*, "High-throughput ion-implantation for low-cost high-efficiency silicon solar cells," *Energy Procedia*, vol. 15, pp. 10–19, 2012.
- [6] V. Prajapati, T. Janssens, J. John, J. Poortmans, and R. Mertens, "Diffusion-free high efficiency silicon solar cells," *Prog. Photovoltaics, Res. Appl.*, vol. 21, no. 5, pp. 980–985, 2013.
- [7] R. Low *et al.*, "High efficiency selective emitter enabled through patterned ion implantation," in *Proc. 35th IEEE Photovoltaic Spec. Conf.*, 2010, pp. 1440–1445.
- [8] A. Haarahiltunen, H. Savin, M. Yli-Koski, H. Talvitie, and J. Sinkkonen, "Modeling phosphorus diffusion gettering of iron in single crystal silicon," *J. Appl. Phys.*, vol. 105, no. 2, p. 023510, 2009.
- [9] R. Chen, B. Trzynadlowski, and S. T. Dunham, "Phosphorus vacancy cluster model for phosphorus diffusion gettering of metals in Si," *J. Appl. Phys.*, vol. 115, no. 5, 2014, Art. no. 054906.
- [10] T. Mchedlidze and M. Kittler, "Involvement of iron-phosphorus complexes in iron gettering for n-type silicon," *Phys. Status Solidi (a)*, vol. 203, no. 4, pp. 786–791, 2006.
- [11] M. Syre, S. Karazhanov, B. Olaisen, A. Holt, and B. Svensson, "Evaluation of possible mechanisms behind P gettering of iron," *J. Appl. Phys.*, vol. 110, no. 2, 2011, Art. no. 024912.
- [12] J. Schön *et al.*, "Main defect reactions behind phosphorus diffusion gettering of iron," *J. Appl. Phys.*, vol. 116, no. 24, 2014, Art. no. 244503.
- [13] A. Peral, A. Dastgheib-Shirazi, H. Wagner, G. Hahn, and C. del Cañizo, "Effect of electrically inactive phosphorus versus electrically active phosphorus on iron gettering," *Energy Procedia*, vol. 77, pp. 311–315, 2015.
- [14] W. Schröter *et al.*, "Phosphorus diffusion gettering of metallic impurities in silicon: mechanisms beyond segregation," *Solid State Phenom.*, vol. 95, pp. 527–538, 2003.
- [15] H. Hieslmair, L. Mandrell, M. Chun, I. Latchford, and B. Adibi, "Advantages of ion-implantation for solar cells," in *Proc. 25th Eur. Photovoltaic Sol. Energy Conf. Exhib.*, 2011, p. 1252.
- [16] D. Macdonald, P. N. Deenapanray, and S. Diez, "Onset of implant-related recombination in self-ion implanted and annealed crystalline silicon," *J. Appl. Phys.*, vol. 96, no. 7, pp. 3687–3691, 2004.
- [17] A. E. Morishige *et al.*, "Combined impact of heterogeneous lifetime and gettering on solar cell performance," *Energy Procedia*, vol. 77, pp. 119–128, 2015.
- [18] J. Hofstetter *et al.*, "Sorting metrics for customized phosphorus diffusion gettering," *IEEE J. Photovoltaics*, vol. 4, no. 6, pp. 1421–1428, Nov. 2014.
- [19] V. Vähänissi, A. Haarahiltunen, M. Yli-Koski, and H. Savin, "Gettering of iron in silicon solar cells with implanted emitters," *IEEE J. Photovoltaics*, vol. 4, no. 1, pp. 142–147, Jan. 2014.
- [20] A. Haarahiltunen *et al.*, "Gettering of iron in silicon by boron implantation," *J. Mater. Sci.—Mater. Electron.*, vol. 19, no. 1, pp. 41–45, 2008.
- [21] T. Buck, K. Pickar, J. Poate, and C.-M. Hsieh, "Gettering rates of various fast-diffusing metal impurities at ion-damaged layers on silicon," *Appl. Phys. Lett.*, vol. 21, no. 10, pp. 485–487, 1972.
- [22] T. Kuroi *et al.*, "Proximity gettering of heavy metals by high-energy ion implantation," *Jpn. J. Appl. Phys.*, vol. 32, no. 1S, p. 303, 1993.
- [23] S. Myers, G. Petersen, and C. Seager, "Binding of cobalt and iron to cavities in silicon," *J. Appl. Phys.*, vol. 80, no. 7, pp. 3717–3726, 1996.
- [24] D. P. Fenning *et al.*, "Iron precipitation upon gettering in phosphorus-implanted Czochralski silicon and its impact on solar cell performance," in *Proc. 40th IEEE Photovoltaic Spec. Conf.*, 2014, pp. 3641–3643.
- [25] A. Haarahiltunen, H. Väinölä, O. Anttila, M. Yli-Koski, and J. Sinkkonen, "Experimental and theoretical study of heterogeneous iron precipitation in silicon," *J. Appl. Phys.*, vol. 101, no. 4, 2007, Art. no. 043507.
- [26] V. Vähänissi, A. Haarahiltunen, H. Talvitie, M. Yli-Koski, and H. Savin, "Impact of phosphorus gettering parameters and initial iron level on silicon solar cell properties," *Prog. Photovoltaics, Res. Appl.*, vol. 21, no. 5, pp. 1127–1135, 2013.
- [27] J. Hyvärinen and J. Karila, "New analysis method for crystalline silicon solar cells," in *Proc. 3rd World Conf. Photovoltaic Energy Convers.*, Osaka, Japan, 2003, pp. 1521–1524.
- [28] Z. Cai *et al.*, "Performance of a high-resolution X-ray microprobe at the Advanced Photon Source," in *Proc. AIP Conf. Proc.*, Stanford, CA, USA, 1999, pp. 31–34.
- [29] D. P. Fenning *et al.*, "Precipitated iron: A limit on gettering efficacy in multicrystalline silicon," *J. Appl. Phys.*, vol. 113, no. 4, 2013, Art. no. 044521.
- [30] D. P. Fenning\*, A. S. Zuschlag\* *et al.*, "Improved iron gettering of contaminated multicrystalline silicon by high-temperature phosphorus diffusion," *J. Appl. Phys.*, vol. 113, no. 21, 2013, Art. no. 214504, \*Equal contributions.
- [31] W. Shockley and W. Read Jr, "Statistics of the recombinations of holes and electrons," *Phys. Rev.*, vol. 87, no. 5, p. 835, 1952.
- [32] S. Grover, J. Li, D. Young, P. Stradins, and H. Branz, "Reformulation of solar cell physics to facilitate experimental separation of recombination pathways," *Appl. Phys. Lett.*, vol. 103, no. 9, 2013, Art. no. 093502.
- [33] A. Hähnel *et al.*, "Electron microscope verification of prebreakdown-inducing  $\alpha$ -FeSi<sub>2</sub> needles in multicrystalline silicon solar cells," *J. Appl. Phys.*, vol. 113, no. 4, 2013, Art. no. 044505.
- [34] J. Thibault *et al.*, "Structure and characterization of the dislocations in tilt grain boundaries between  $\Sigma = 1$  and  $\Sigma = 3$ ; a high resolution electron microscopy study," *Mater. Sci. Eng., A*, vol. 164, no. 1, pp. 93–100, 1993.
- [35] O. Breitenstein, J. P. Rakotoniaina, M. H. Al Rifai, and M. Werner, "Shunt types in crystalline silicon solar cells," *Prog. Photovoltaics, Res. Appl.*, vol. 12, no. 7, pp. 529–538, 2004.



- [36] O. Breitenstein *et al.*, "Understanding junction breakdown in multicrystalline solar cells," *J. Appl. Phys.*, vol. 109, no. 7, 2011, Art. no. 071101.
- [37] D. Gilles, W. Schröter, and W. Bergholz, "Impact of the electronic structure on the solubility and diffusion of 3d transition elements in silicon," *Phys. Rev. B*, vol. 41, no. 9, p. 5770, 1990.
- [38] S. Myers, M. Seibt, and W. Schröter, "Mechanisms of transition-metal gettering in silicon," *J. Appl. Phys.*, vol. 88, no. 7, pp. 3795–3819, 2000.
- [39] T. Buonassisi *et al.*, "Synchrotron-based investigations of the nature and impact of iron contamination in multicrystalline silicon solar cells," *J. Appl. Phys.*, vol. 97, no. 7, 2005, Art. no. 074901.
- [40] J. Hofstetter, D. P. Fenning, J.-F. Lelièvre, C. del Cañizo, and T. Buonassisi, "Engineering metal precipitate size distributions to enhance gettering in multicrystalline silicon," *Phys. Status Solidi (a)*, vol. 209, no. 10, pp. 1861–1865, 2012.
- [41] A. E. Morishige *et al.*, "Building intuition of iron evolution during solar cell processing through analysis of different process models," *Appl. Phys. A*, vol. 120, no. 4, pp. 1357–1373, 2015.
- [42] H. Hieslmair *et al.*, "Gettering of iron by oxygen precipitates," *Appl. Phys. Lett.*, vol. 72, no. 12, pp. 1460–1462, 1998.
- [43] J. Wong-Leung *et al.*, "The precipitation of Fe at the Si-SiO<sub>2</sub> interface," *J. Appl. Phys.*, vol. 83, pp. 580–584, 1998.
- [44] J. D. Murphy and R. J. Falster, "Contamination of silicon by iron at temperatures below 800 °C," *Phys. Status Solidi—Rapid Res. Lett.*, vol. 5, nos. 10/11, pp. 370–372, 2011.
- [45] J. Schön, H. Habenicht, M. Schubert, and W. Warta, "Understanding the distribution of iron in multicrystalline silicon after emitter formation: Theoretical model and experiments," *J. Appl. Phys.*, vol. 109, no. 6, 2011, Art. no. 063717.
- [46] P. Plekhanov and T. Tan, "Schottky effect model of electrical activity of metallic precipitates in silicon," *Appl. Phys. Lett.*, vol. 76, no. 25, pp. 3777–3779, 2000.
- [47] M. Negoita and T. Tan, "Metallic precipitate contribution to generation and recombination currents in p-n junction devices due to the Schottky effect," *J. Appl. Phys.*, vol. 94, no. 8, pp. 5064–5070, 2003.
- [48] W. Kwapił, J. Schön, W. Warta, and M. C. Schubert, "Carrier recombination at metallic precipitates in p-and n-type silicon," *IEEE J. Photovoltaics*, vol. 5, no. 5, pp. 1285–1292, Sep. 2015.
- [49] J. Schmidt *et al.*, "Impurity-related limitations of next-generation industrial silicon solar cells," *IEEE J. Photovoltaics*, vol. 3, no. 1, pp. 114–118, Jan. 2013.
- [50] S. Rein, *Lifetime Spectroscopy: A Method of Defect Characterization in Silicon for Photovoltaic Applications*. New York, NY, USA: Springer, 2006.
- [51] S. M. Sze and K. K. Ng, *Physics of Semiconductor Devices*. New York, NY, USA: Wiley, 2006.
- [52] J. Hofstetter, C. Cañizo, H. Wagner, S. Castellanos, and T. Buonassisi, "Material requirements for the adoption of unconventional silicon crystal and wafer growth techniques for high-efficiency solar cells," *Prog. Photovoltaics, Res. Appl.*, vol. 24, no. 1, pp. 122–132, 2016.
- [53] A. Liu, C. Sun, and D. Macdonald, "Hydrogen passivation of interstitial iron in boron-doped multicrystalline silicon during annealing," *J. Appl. Phys.*, vol. 116, no. 19, 2014, Art. no. 194902.
- [54] P. Karzel, A. Frey, S. Fritz, and G. Hahn, "Influence of hydrogen on interstitial iron concentration in multicrystalline silicon during annealing steps," *J. Appl. Phys.*, vol. 113, no. 11, 2013, Art. no. 114903.
- [55] J.-F. Lelièvre *et al.*, "Dissolution and gettering of iron during contact co-firing," *Energy Procedia*, vol. 8, pp. 257–262, 2011.
- [56] A. Istratov, H. Hieslmair, and E. Weber, "Iron and its complexes in silicon," *Appl. Phys. A*, vol. 69, no. 1, pp. 13–44, 1999.
- [57] M. Aoki, A. Hara, and A. Ohsawa, "Fundamental properties of intrinsic gettering of iron in a silicon wafer," *J. Appl. Phys.*, vol. 72, no. 3, pp. 895–898, 1992.
- [58] J. Schön *et al.*, "Analyses of the evolution of iron-silicide precipitates in multicrystalline silicon during solar cell processing," *IEEE J. Photovoltaics*, vol. 3, no. 1, pp. 131–137, Jan. 2013.

Authors' photographs and biographies not available at the time of publication.